Swiss Accelerator Research and Technology

CHART Scientific Report

FCC-ee High-Temperature-Superconducting Short Straight Section

(FCCee HTS4)

PSI:
Michael Koratzinos, Bernhard Auchmann, André Brem, Matteo Crescenti, Micha! Duda, Jaap Kosse, Kirtana Puthran, Jürgen Schmidt

CERN:
Francesco Bardi, Ioannis Dimoulios

29.04.2026

Technical Report: HTS4 Cos-Theta Demonstrator

CONTENTS

I. INTRODUCTION

The baseline FCC-ee main storage ring magnet configuration consists chiefly of iron-dominated normal conducting dipoles, quadrupoles and sextupoles[1]. The latter two form the short straight sections and consume a large amount of power (up to 79 MW[2]). By replacing the normal-conducting quadrupoles and sextupoles by HTS-based systems, several benefits can be obtained: significant power savings (from 79 MW down to 12 MW), an increase in dipole filling-factor, and flexibility in the optics design[3]. The power savings result from a reduction in dissipation in the magnets as well as from a reduction in synchrotron radiation due to the increased dipole filling factor (which increases the effective bending radius). Demonstrating the advantages and feasibility of HTS-based short straight sections (SSS) is the goal of the CHART project HTS4.

Key to the energy-efficient operation of the HTS magnet system is the operation at relatively high temperatures (around 40 K), required to keep the power consumption of the cryogenic system low. The optimum operating conditions follow from balancing operational costs with capital expenditure. Elements to the solution are: magnets with efficient conductor use and low component cost, cost-effective and operationally efficient, a highly reliable cryogenic system[4], a powering concept that minimizes heat input at the leads[5] while ensuring high system availability, and a beam dynamics concept that takes full advantage of the new coil arrangement.

As part of the HTS4 initiative, a cosine-theta configuration sextupole demonstrator magnet, designated *Ozzy*, has been designed, constructed, and tested. The cosine-theta geometry refers to a winding pattern where the current-density in the cross-section follows a (co)sinusoidal distribution around the magnet bore, providing optimal magnetic field shaping for multi-pole magnets while maximizing conductor utilization efficiency. This demonstrator represents a proof-of-concept for the feasibility of HTS magnet technology in high-energy physics applications, addressing key technical challenges including coil manufacturing, cryogenic operation, and electrical performance under realistic operating conditions. Field quality will be addressed in the next stage of the project, where a longer nested sextupole/quadrupole magnet will be delivered for a full evaluation of FCC-ee design specifications.

The REBCO demonstrator uses a 4 mm tape with self-bonding coating technology, allowing for post-winding coil curing, and providing a controlled turn-to-turn resistivity. The resistivity value is tuned to reproduce steel-tape metal insulation, which has been proven to provide intrinsic quench protection for magnets of a similar class. The magnet was designed for operation at 40 K with current capacity up to 365 A. It features comprehensive instrumentation for voltage measurement across individual coils and splice joints, alongside Hall sensor arrays in the magnet bore for first-order magnetic field characterization.

This report presents the complete development and testing of the HTS4 cos-theta demonstrator magnet conducted in 2025, encompassing design, manufacturing, and comprehensive electrical characterization from 20 K to 70 K. Section II details the electromagnetic and mechanical design considerations that guided the development of the demonstrator. Section IV describes the partial insulation coating processes, automated winding techniques, thermal curing procedures, splice connections, and vacuum impregnation used in magnet construction. Section V presents the experimental results including instrumentation setup, electrical performance characterization under nominal operating conditions of 40 K, temperature-dependent critical current measurements and analysis of electromagnetic decay time. Section VI summarizes the development and test results of the demonstrator and provides perspectives for future work in the project.

This work was performed under the auspices of and with support from the Swiss Accelerator Research and Technology (CHART) program (www.chart.ch).

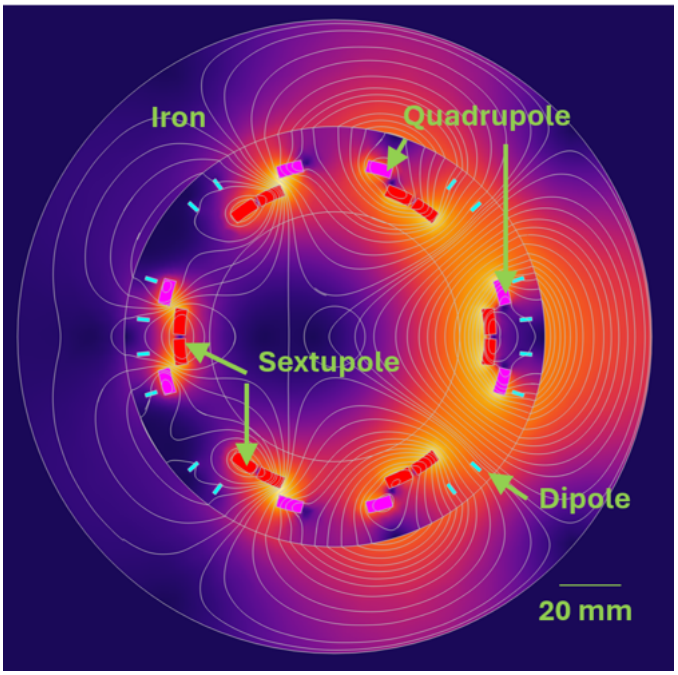

Fig. 1: Example of a cross-section of fully-nested HTS short straight section based on a sextupole, quadrupole and dipole, formed by an assembly of cosine-theta coils.

TABLE I: Maximum required integrated strength per harmonic per short section, at a 10 mm reference radius[6]. White-backgrounds indicate requirements, yellow backgrounds indicate derived values or design choices.

Harmonic	$\lvert\int B_n \mathrm{d}z\rvert$ [Tm]	L_{mag} [m]	$\lvert B_n\rvert$ [T]
Dipole (SSS)	0.1459	2.9	0.0503
Quadrupole	0.3439	2.9	0.1186
Sextupole	0.1345	2.7	0.0498
Hor. dip corrector	0.0174	2.9	0.006
Vert. dip corrector	0.0174	TBD	TBD
Skew quadrupole	0.0058	TBD	TBD

II. Design

A. Requirements

The electromagnetic design of the sextupole is based on a potential short straight section implementation involving a nested sextupole and quadrupole configuration; eventually also including a nested dipole, which would render the short straight sections curved. Here 'nested' means that the magnets share the same axial space. The short sections formed by these quadrupoles and sextupoles (and ultimately dipoles) form the double-aperture main ring together with normal-conducting dipoles. There would be around 2900 short straight sections. By including nested HTS dipoles with the quadrupole and sextupole, we aim at a 100% dipole filling factor.

Replacing the normal-conducting sextupoles and quadrupoles with HTS variants, and ensuring a high dipole filling factor could be achieved via two implementations. One could either put a nested dipole/quadrupole in sequence with a nested dipole/sextupole or fully nest all three harmonics, meaning the magnets share the same axial space. Since the required magnetic field ratios vary for different operating modes, combined function coils are unsuitable. The quadrupole cannot be shorter than 2.9 m due to synchrotron radiation considerations[3]. This means that a dipole+quadrupole in series with a dipole+sextupole will result in a longer magnet than a fully nested system. The advantage of such an approach would be that it avoids the superposition of field of the different coil sets on each other would be less. For the conceptual study, we chose the fully nested configuration.

Requirements on magnets for a short straight section based on nested magnets and a maximized dipole filling factor are listed in[6]. The magnetic field strength that each harmonic set needs to generate is relatively modest, leading to peak fields on the windings of around 2 T. The magnetic field profile in the bore of a combination of dipole, quadrupole, and sextupole components can be expressed as a strength B_1, B_2, B_3, respectively. This is achieved by performing a Fourier expansion at a certain reference radius[7], in this case 10 mm. The maximum required strengths are defined by the operation in the highest energy mode, $t\bar{t}$[1].

From the integrated strength requirements, listed in Table I, the strengths are derived as follows: the quadrupole minimum magnetic length is fixed by synchrotron radiation limits, and we set the quadrupole length to this minimum (2.9 m). The dipole ideally covers as much length as possible, so it is set to the same length as the quadrupole. The sextupole is set slightly shorter, to 2.7 m, to allow axial space for other correction coils.

The sextupoles in each short straight section need to be able to be independently set and may have a negative or positive polarity. At the moment, there is no expectation that the sextupoles in both beam lines have the same strength or polarity.

A nested dipole belonging to a defocused quadrupole has the same strength requirement as the main dipoles, but a dipole nested with a focused quadrupole only requires 53% of the strength[3], due to higher-order effects of the quadrupole on the beam trajectory. This makes it desirable to have the quadrupoles for both beams within a given short section provide the same function (i.e. either focus or defocus), as that allows both dipoles in one short section to have the same strength and thus be powered by the same power supply.

As a given quadrupole might have a defocusing role in Z-mode, and focusing in $t\bar{t}$-mode, whereas its dipole always generates a positive field, this makes combined function magnets, in which one coil set generates multiple harmonics, unattractive for this particular application.

As we judged that out of the 3 harmonics (B_1/B_2/B_3) the sextupole would be the most difficult magnet from a manufacturing perspective, for a first demonstrator this would be the harmonic to try to build.

There are three main reasons why we propose a cosine-theta geometry for all three coil-sets.

- The cosine-theta, neglecting the possible advantages of field-aligned configurations, is the most conductor-efficient coil type, and it enables efficient nesting of various multi-pole arrangements, similar to LHC nested corrector-magnet.

TABLE II: Comparison of full-scale SSS and demonstrator

Parameter	Unit	SSS	Demonstrator
No. of sextupole turns per cross-section (1 aperture)		492	492
No. of quadrupole turns per cross-section (1 aperture)		240	0
No. of dipole turns per cross-section (1 aperture)		80	0
Sextupole current	A	320	370
Quadrupole current	A	320	0
Dipole current	A	67	0
Iron yoke		yes	no
B_3 at 10 mm radius	mT	50	50
B_2 at 10 mm radius	mT	120	0
B_1 at 10 mm radius	mT	51	0
Current sharing temperature T_{cs}	K	40	40
Conductor		ReBCO	ReBCO

TABLE III: Parameters of the HTS4 cos-theta demonstrator magnet

Parameter	Value
No. of turns per coil	82
No. of coils	6
Tape length per coil (m)	34
Minimum bending radius (mm)	16
Straight section length (mm)	110
Operating current (A)	365
Sextupole field strength (mT)	49.8
Peak field on conductor (T)	2.2
Inductance (mH/m)	54.8
Maximum torsion (1/m)	67
Maximum normal curvature (1/m)	95
Maximum geodesic curvature (1/m)	16

- A cosine-theta geometry does not need a complex winding mandrel, saving costs.
- The winding of the cosine-theta coils, as will be demonstrated in this report, can be automated.

B. Electromagnetic Design

In addition to the goal of generating a sextupole component of 0.0498 T, an additional constraint we placed on the sextupole was a current sharing temperature of 40 K. This resulted from an optimization of the operating temperature and adding a temperature margin to that. This optimization balances operational costs (dominated by electricity use required for cooling of the superconductor) and capital costs (dominated by the superconducting tape). This optimization is not part of this document. An additional result from the optimization is that 4 mm wide tape is preferred over the other commercially available options (2 mm and 12 mm). Moreover, from the necessity to include between the beam wall and the sextupole 1) a cryostat wall, 2) multi-layer insulation, 3) an inner mandrel on which the coil is attached, a minimum inner sextupole radius of 49 mm is derived.

As a side note, when the project started, an operating temperature of 40 K, an operating current of 250 A and a targeted sextupole field of 40 mT was foreseen. The two specifications are compatible, i.e., the demonstrator would meet these specs if an iron yoke were introduced.

The REBCO tape used in the demonstrator is produced by Faraday Factory Japan. The tape width is 4 mm, Hastelloy thickness 38 µm, copper thickness 20 µm/side. The two spools used have an average Ic (77 K, S.F.) of 237.1 A and 235.2 A, with standard deviation 4.9 A and 3.35 A. To estimate the expected performance of the sextupole, a scaling law of the form proposed by[8] is used. The $I_c(B, T, \theta)$ behavior of the tape is taken from[9,10] and represents SuperOx YBCO tape[1]. A scaling factor is used to match the 77 K self-field performance of the actual tape, as measured by the manufacturer.

As a first step towards the sextupole design, the 2D field quality was investigated. The effects of screening currents are not part of this analysis. It was found that one could already achieve decent magnetic field quality (unwanted terms smaller than 1 unit) by using just one conductor block per pole. This could in reality be achieved by 3 coils, whose legs would form the 6 poles of the sextupole. Subdivision of the poles is not required to meet the magnetic field quality targets (<1 unit). This follows from the small relative ratio of the harmonic reference radius (10 mm) to the sextupole inner radius (49 mm). The choice was made to subdivide each pole into 2 blocks (Figure 1), as this would result in a 6-coil sextupole, with the advantage that the hard-way bending in the coil-end would be smaller than for a 3-coil configuration. The coils ends were optimized in ROXIE to reduce the hard-way bending as much as possible.

The quadrupole poles are split into two blocks per pole, realizable with 4 coils (Figure 1). The dipole on the other hand was found to require more subdivision, with 4 blocks per pole yielding good field quality.

Whereas a full-scale SSS would feature two apertures, and iron shielding to reduce the cross-talk between different apertures' magnets, it was decided to omit iron for the sub-scale demonstrator.

The turn-to-turn resistance of the coils is aimed to be in the same range as metal-insulated coils[11], but relies on a self-bonding coating layer instead of on contact pressure between turns. The inspiration for our coating comes from the wire industry[12]. There, the metal wire is covered first by the actual electrical insulation layer, on top of which the bonding layer is applied. Winding packs wound from this type of wire can be fused into a solid piece by either solvent-based or heat-based bonding. Our idea is to skip the typical insulation layer, and to

[1]Tape with similar performance is obtainable from Faraday Factory Japan.

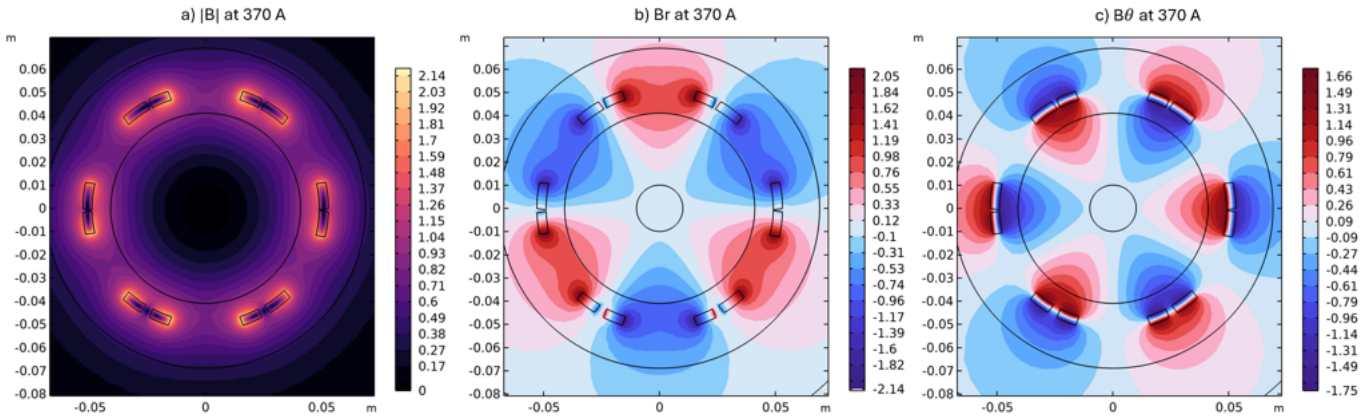

Fig. 2: Sextupole demonstrator magnetic field distribution a) norm, b) radial component, c) azimuthal component, at a current of 370 A.

achieve a desired contact resistance by applying a conductive bonding layer directly around the conductor.

If instead the coil would be wound from insulated tape, protected by external discharge over a dump resistor, the copper thickness of 20 µm/side would not have been sufficient to prevent excessive temperatures, if a quench would occur at 365 A. The inclusion of additional copper, as well as the insulation thickness itself (15 µm/side) would result in thicker turns, and thus in more of the turns being placed in less-effective areas, leading to a higher required number of turns per coil. As an example, a set of 6 coils at 320 A based on 100 µm thick turns would need 78 turns per coil, whereas with 140 µm thick turns, 85 are needed.

The key design parameters for the HTS4 cos-theta demonstrator magnet are summarized in Table III. The next section describes the mechanical assembly of the demonstrator.

III. Mechanical Assembly

This section describes the mechanical aspects of the coil configuration and the structural elements that form the complete magnet assembly

A. Coil Configuration

The magnet features six individual coils arranged in cos-theta geometry and positioned concentrically around a central bore with an outer diameter of 98 mm. Figure 3a shows the coil configuration on the central bore. The six coils are positioned on this bore using placement pins to ensure accurate angular and radial alignment.

The coils are connected in series. Two types of electrical connections link the coils: outer splices connect via the outermost turn, whereas inner splices use the first turn, through copper blocks and 12 mm HTS tape segments. The current flows from the first turns via the copper block to the 12 mm segments. Each coil has 82 turns, 110 mm straight sections and a minimum bending radius of 16 mm. The coil structure follows the cosine-theta pattern essential for generating the required sextupole field distribution. Figure 4 illustrates the three-dimensional coil geometry with orthogonal projections showing dimensional details.

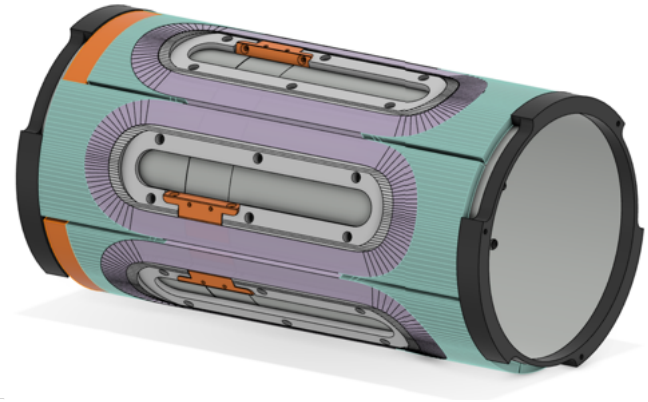

(a) Individual coils connected in series through inner and outer splices to form the sextupole magnet configuration on the magnet bore.

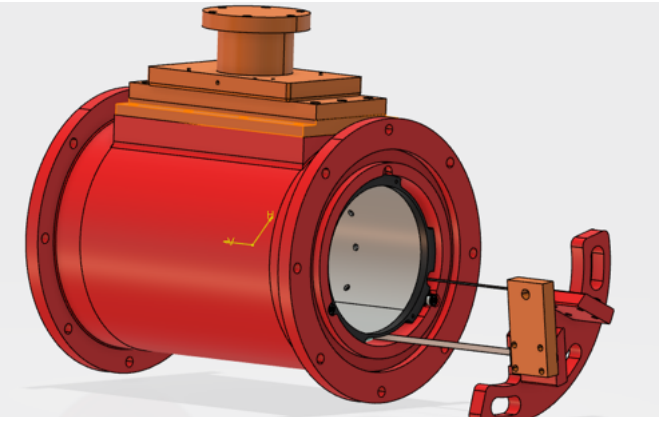

(b) Complete magnet assembly showing aluminum shell, current leads, and cryostat connection blocks.

Fig. 3: CAD images of the magnet assembly, showing the coil configuration and structural integration. The cos-theta coil arrangement uses placement pins for accurate alignment, while the complete assembly features aluminum shell containment with current leads and thermal interface connections.

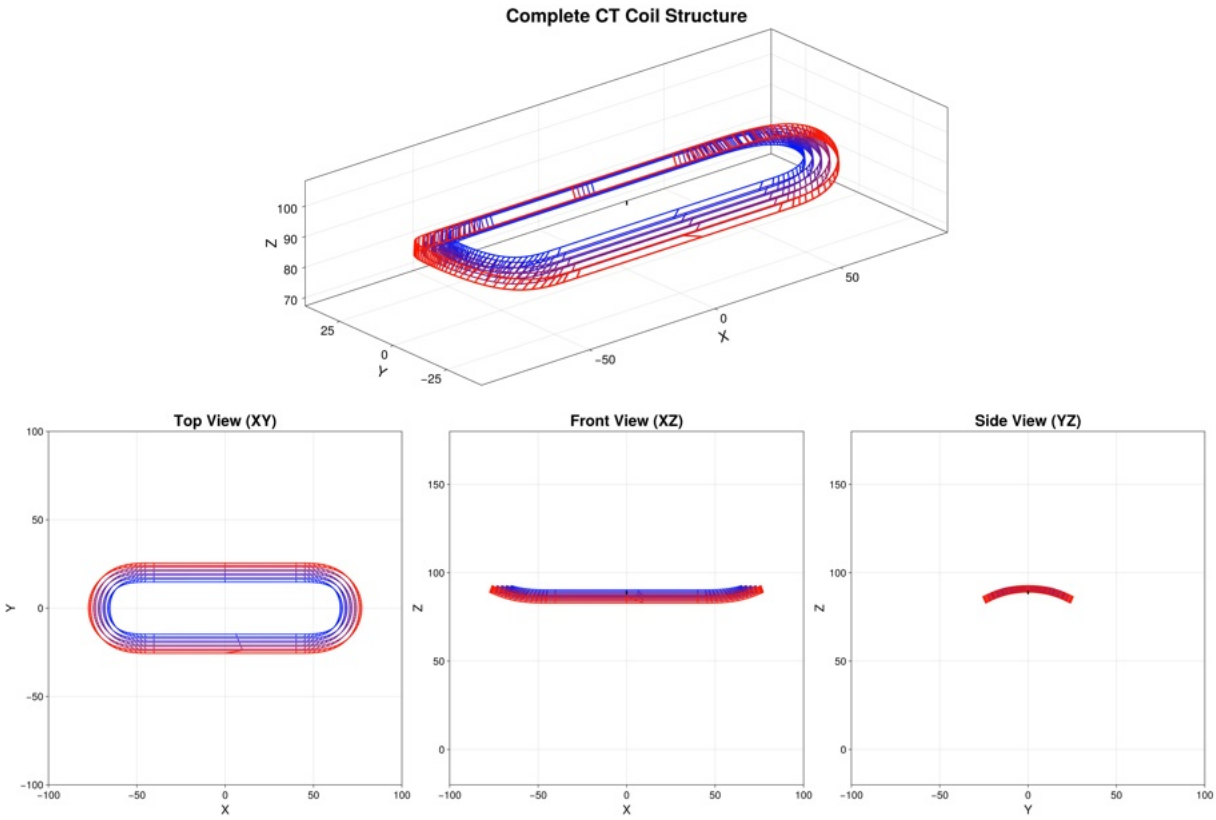

Fig. 4: Cos-theta coil structure geometry showing conductor arrangement with a few individual turns visible in 3D view and orthogonal projections displaying coil dimensions.

B. Assembly Configuration

The complete assembly configuration is shown in Figure 3b. The inner stainless steel bore with the assembled coils are inserted into an aluminum alloy shell. The shell provides the primary structural containment for the coil assembly. Once positioned within the shell, the coil assembly undergoes vacuum impregnation with alumina-filled wax. This impregnation process occurs with the coils already installed in their final positions within the aluminum containment, creating a mechanically rigid composite structure. The wax provides thermal conduction pathways and distributes mechanical loads uniformly across the assembly. Aluminum was chosen as a compromise between costs and thermal conductivity.

The current leads of the magnet extend from the (respective end-) coil terminals through dedicated feed-through points in the shell wall. These leads are visible in Figure 3b and provide electrical connection to external circuits while minimizing thermal conduction. The voltage tap instrumentation feed-through (not shown in the figure) ports enable individual coil and splice joint monitoring during electrical characterization. The copper connection blocks mounted on top of the exterior Al shell are a mechanical and thermal interface with the cryostat system with mounting points for heaters. Electrical isolation is maintained using thermal conductive insulating epoxy.

The complete assembly maintains mechanical stability across the full operating temperature range from 15 K to 77 K during testing through careful material selection and joint design that accommodate differential thermal contraction.

IV. Manufacturing

The manufacturing process of the magnet follows a sequential five-stage approach comprising 1) coating of the HTS tapes, 2) winding of the coils from the coated tape, 3) thermal curing of the partial insulation, 4) introduction of electrical connections and instrumentation, and 5) wax impregnation.

A. Coating Process

The coating process employs a continuous dip-coating methodology [13] utilizing polyvinyl butyral (PVB) as the thermoplastic matrix with graphite powder as conductive fillers. The coating composition consists of 30 v% graphite powder in low molecular weight PVB dissolved in acetone solvent at 12.5 v% concentration, providing controlled viscosity for uniform layer deposition. The coating formulation, developed for the HTS4 project targets turn-to-turn contact resistance values above $100\,\mu\Omega \cdot cm^2$ while maintaining processing characteristics favorable for large-scale coil manufacturing applications. Figure 5a shows the dip-coating process setup, and an image of the coated HTS coated tape is shown in Figure 5b. The coating process employs continuous stirring of the bath solution to maintain homogeneous filler dispersion and infrared heating for solvent evaporation, currently achieving coating thicknesses of 5-20 μm. Due to the characteristic

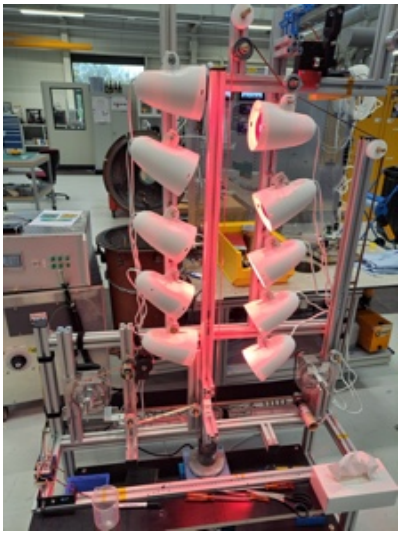

(a) Dip-coating process setup showing continuous tape processing through PVB solution bath with infrared drying section.

(b) Image of PVB-coated HTS tape showing the uncoated edges.

Fig. 5: Novel *partial* - insulation developed in order to tune the quench characteristics of coils

cross-sectional geometry of the HTS tape, the coating does not cover the tape edges. This effect does not seem detrimental to the coil performance.

B. Winding of coils

The winding process is carried out on a 5-axis winding machine shown in Figure 6 with coordinated control of vertical rotation (V-axis), horizontal rotation (H-axis) of the beam, as well as longitudinal (X-axis), vertical positioning (Z-axis), and tape rotation (R-axis) of the pay-off. The winding process represents a control problem due to the non-planar coil geometry. It requires simultaneous coordination of five machine axes to maintain optimal tape contact and alignment at each winding position.

A program has been written in Julia programming language to address the winding problem. The algorithm of the program transforms the coil surface geometry into machine-readable coordinates through systematic coordinate transformations and optimization calculations. Considering an angular rotation of the winding beam (typically 42 steps per 360^o), the algorithm identifies the target surface element with maximum radial extent after V-axis rotation, then calculates the corresponding H-axis angle required to align the surface tangent with the horizontal plane for optimal tape contact. The payoff head position is calculated from the surface normal vector projection to ensure the tape width aligns perpendicular to the surface curvature, preventing tape edge lifting during application. A visual representation of this calculation is shown in Figure 7. The program also accounts for the varying coil radius and surface orientation throughout the winding process. The resulting sequence data includes all five machine coordinates (V, H, X, Z, R) along with process parameters such as winding speed and tension values, formatted as CSV output compatible with the control system of the winding machine.

The automation system successfully generates complete winding sequences for the cos-theta geometry, eliminating manual winding and ensuring consistent tape placement across all the turns of each coil.

During the winding operation, the initial 25 - 30 turns of a coil are completed without additional tooling support. After this, anodized aluminum clamping fixtures are installed, shown in Figure 8, are used to provide lateral support as the coil diameter increases with successive winding layers. The clamping fixtures requires incremental repositioning to accommodate the growing coil geometry while maintaining the continuous winding process. The coils are wound with a maximum tension of 35 N on the tape.

C. Curing of partial insulation

Upon completion of winding, additional anodized aluminum tooling are used to hold the coil assembly from the sides for the thermal curing operation of the coating. The curing process involves a controlled thermal treatment up to 175°C, which fuses the coating from adjacent turns together, yielding a monolithic winding pack. The heat treatment duration and temperature are based on target contact resistance specifications. All tooling components feature anodized surfaces in order provide electrical isolation of the coils. This enables *in-situ* measurement of coil resistance throughout the curing and ensures reproducibility of the turn-turn contact resistance of different coils. Figure **??** shows the assembly configuration of the coil for the curing process. The resulting monolithin coil pack is seen in Figure 9b.

Figure 10 demonstrates the evolution of temperature and coil-resistance with time during a representative curing cycle. During the development phase of the partial insulation methodology, four prototype coils not incorporated into the final magnet assembly were subjected to qualification testing. These development coils underwent multiple thermal cycling sequences between room temperature and liquid nitrogen temperature (77 K) with no observable performance degradation or structural deterioration, arising from the curing process. These measurements confirm the long-term stability and reliability of

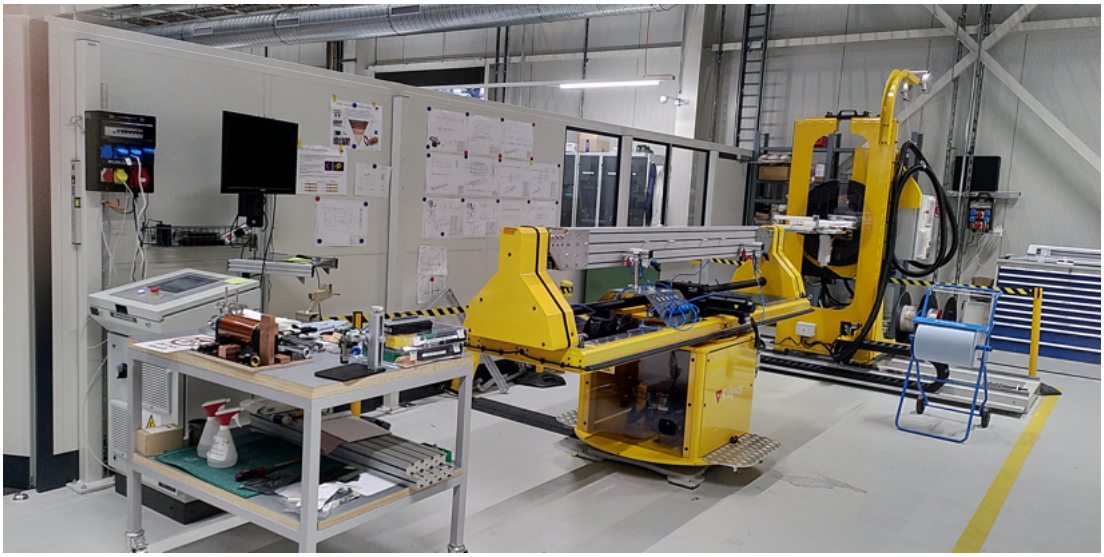

Fig. 6: 5-axis winding machine used for automated cos-theta coil fabrication, showing the coordinated control system for V-axis (vertical rotation), H-axis (horizontal rotation), X-axis (longitudinal positioning), Z-axis (vertical positioning), and R-axis (tape rotation).

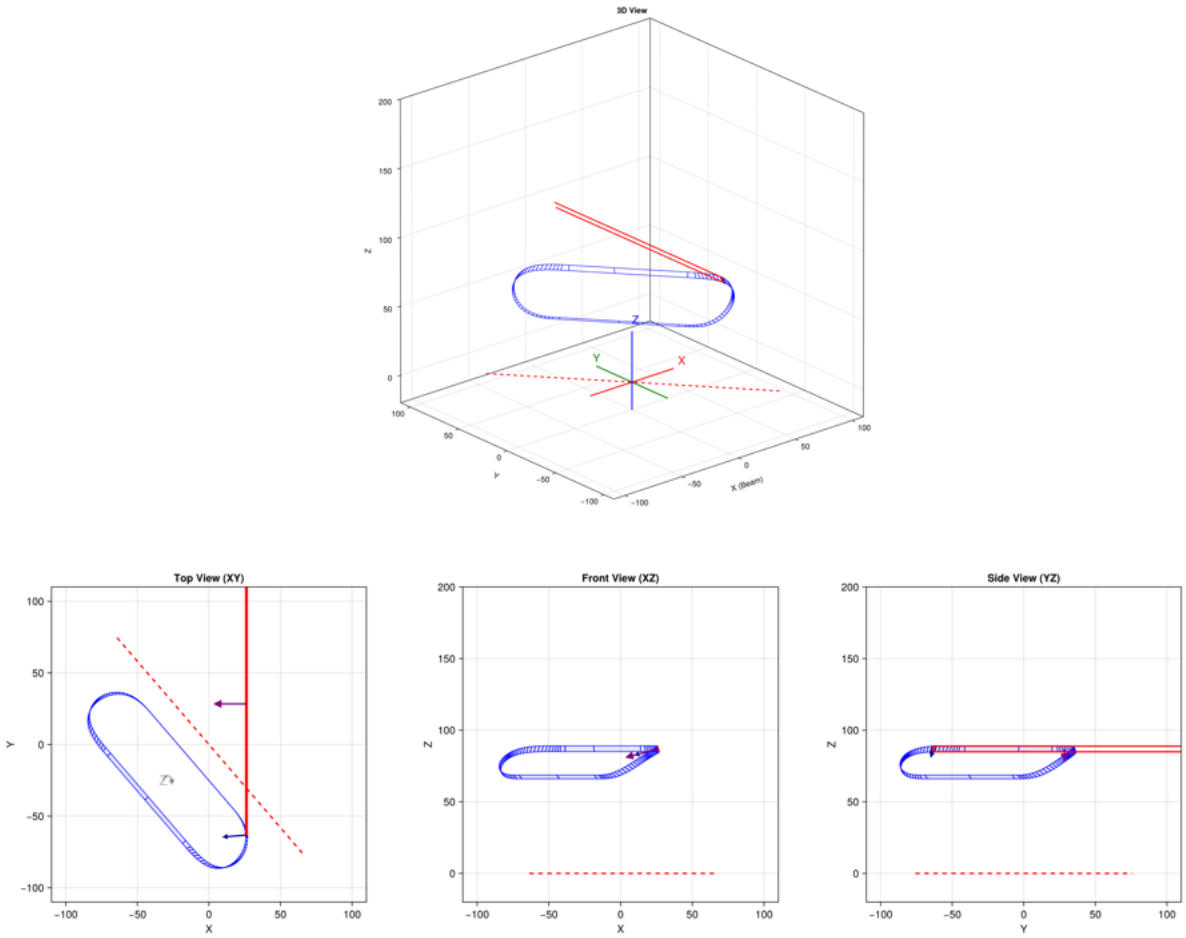

Fig. 7: Example winding position showing the coordination of all five machine axes in the global coordinate axes. The projections illustrate how the three-dimensional surface geometry is mapped to specific machine coordinates for this winding step.

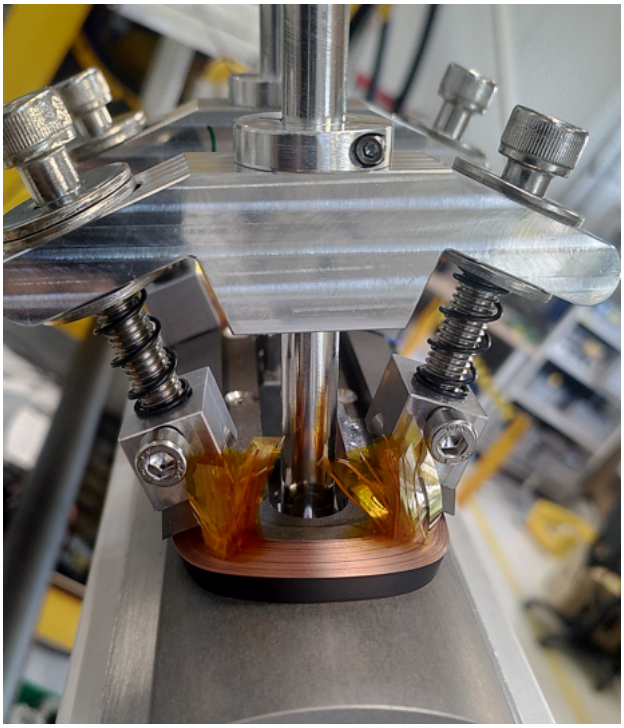

Fig. 8: Anodized aluminum clamping fixtures providing lateral support during cos-theta coil winding. The tooling is incrementally repositioned to accommodate growing coil diameter while maintaining automated winding capability throughout the 82-turn process.

the PVB-based partial insulation approach for HTS cos-theta magnet applications.

Turn-to-Turn Contact Resistance Analysis

The turn-to-turn contact resistance represents a critical parameter in partially insulated HTS coils, as it determines the current redistribution characteristics and electromagnetic decay behavior. The contact resistance between adjacent turns can be extracted from total coil resistance measurements through circuit analysis.

For a coil with N turns, the total measured resistance R_{coil} comprises two main components: the intrinsic tape resistance R_{tape} and the turn-to-turn contact resistance network $R_{\perp}$. These components are connected in a parallel configuration, where the tape provides a primary current path and the turn-to-turn contacts provide secondary current redistribution paths. The relationship between these resistances is given by:

$$R_{\perp}^{-1} = R_{\text{coil}}^{-1} - R_{\text{tape}}^{-1} \tag{1}$$

The turn-to-turn resistance network $R_{\perp}$ consists of N individual contact resistances connected in series between adjacent turns. Assuming uniform contact properties, the average turn-to-turn contact resistance per unit area $\bar{R}_{\text{turnturn}}$ can be calculated as:

$$\bar{R}_{\text{turnturn}} = \frac{R_{\perp} \cdot w_{\text{tape}} \cdot \bar{L}_{\text{turn}}}{N} \tag{2}$$

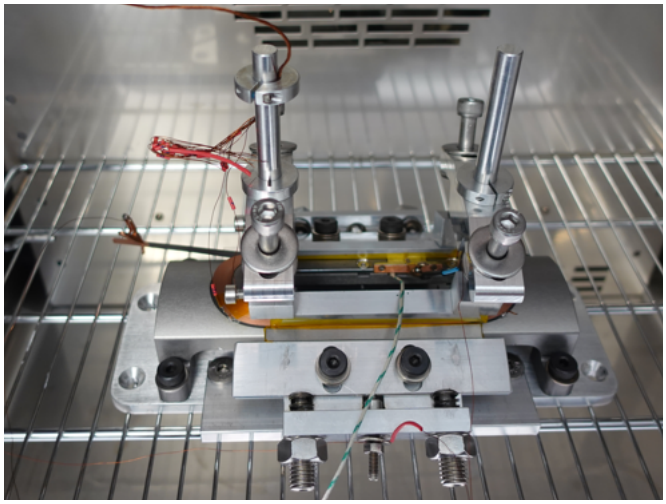

(a) Coil assembly positioned within the curing furnace in preparation for the thermal treatment.

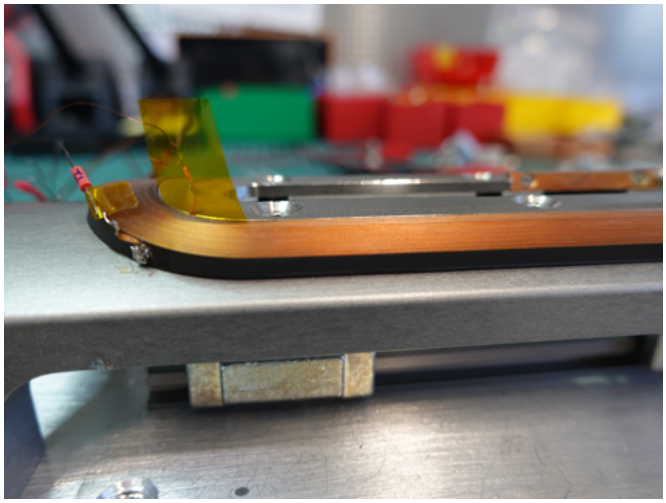

(b) Self-supporting cos-theta coil following thermal curing and tooling removal.

Fig. 9: Thermal curing process of the coating creates mechanically self-supporting coil structures that maintains precise cos-theta coil geometry.

where:

- w_{tape} is the tape width
- $\bar{L}_{\text{turn}} = L_{\text{tot}}/N$ is the average turn length
- L_{tot} is the total conductor length per coil
- N is the number of turns per coil

This estimation allows for indirect determination of the contact resistance properties achieved through the PVB coating and curing process.

The curing cycle involves heating the coils to maximum temperature (typically 175°C) to activate the thermoplastic PVB coating, followed by controlled cooling during which the resistance is monitored in real-time. The coil resistance peaks during the heating phase due to increased electrical resistivity at elevated temperatures, then decreases as the coating fuses and temperature drops. Final resistance values are recorded at room temperature (25°C) after furnace shutdown, providing the baseline electrical characteristics for subsequent low-

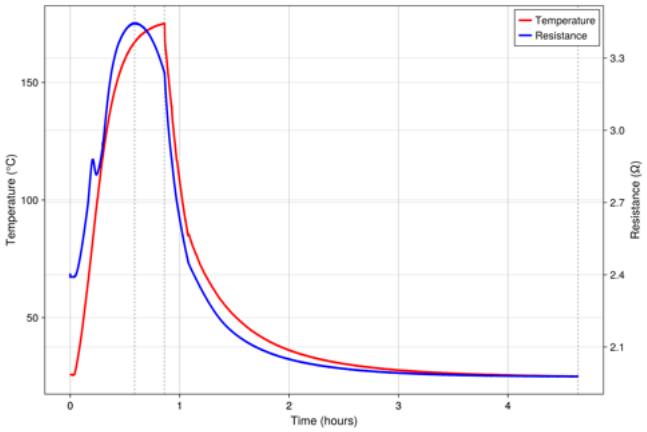

Fig. 10: Temperature and coil resistance monitoring during partial insulation curing, showing resistance development as a function of thermal treatment parameters.

TABLE IV: Individual coil and contact resistances at room temperature following partial insulation curing

Coil	Max Temperature (°C)	Coil Resistance		Turn-Turn Resistance ($\mu\Omega$·cm^2)
		Max Temp* (Ω)	25°C (Ω)	
C1 - Bheema	175	3.24	1.98	1977.7
C2 - Apu	175	3.27	2.12	2117.6
C3 - Kiwi	180	3.25	2.02	2020.7
C4 - Wasabi	177	3.25	2.17	2174.4
C5 - Mochi	175	3.26	2.12	2117.4
C6 - Cookie	178	3.25	2.11	2110.9

*Coil resistance measured when heating of the coil/furnace is shutdown.

temperature operation.

The final coil and contact resistances for each of the six coils used in the demonstrator magnet measured at room temperature is summarized in Table IV, providing baseline electrical characteristics following the curing process.

Although 90 K resistance data were obtained, contact resistance calculation requires temperature-dependent tape resistivity data not currently available. The primary objective during this phase of the project was to develop and demonstrate a process for controlling contact resistance during curing, addressing the challenge of varying tape surface finish over meter-length scales. However, fundamental work during the development of the coating [13] on single tapes shows a factor of 2.5 - 3 difference in the contact resistance of the room temperature measurements compared to that at 77 K. The six coils achieved room temperature coil resistances of 2.09 ± 0.07 Ω and turn-turn contact resistances of 2087 ± 74 $\mu\Omega$·cm^2 .

D. Splice Connections, Current Leads and Instrumentation

Prior to vacuum impregnation, electrical connections between coils are established through joints/splices using 60/40 Sn-Pb solder. As mentioned earlier, the coil interconnections consist of three *inner* splices and two *outer* splices. One each of these can be seen in Figure 11.

The current lead assembly, shown in Figure 12a, provides the electrical interface between the magnet and external power supply. Each current lead consists of a 4 mm HTS tape section soldered in parallel to the outermost turn of the terminal coils, in addition two pre-soldered copper tape segments of the same width. Mechanical reinforcement is provided by 4 mm wide fiberglass supports integrated into the lead structure.

Fig. 11: View of coil showing inner and outer splice connections and voltage tap locations. Inner splices (IS) are fabricated using 12 mm HTS tape segments, while outer splices (OS) connect the coils via the outermost turns. Voltage taps enable individual coil and splice resistance monitoring during testing.

Each coil is also instrumented with voltage taps at the first and last turn, as seen in Figure 11. This allows for the electrical characterization of all the coils and splices. The instrumentation wires are protected with glass fiber and passed through dedicated feed-throughs in the magnet shell. The coil assembly is prepared with a protective polyimide sheet as shown in Figure 12b in preparation for the next operation. This ensures electrical insulation of the coils, voltage taps and splices from the external shell.

E. Vacuum Impregnation

Vacuum impregnation with alumina-filled wax also represents a novel approach to achieving thermo mechanical stability in the HTS cos-theta magnets. Following coil winding and instrumentation, the assembled magnet undergoes the experimental impregnation process. Prior to implementing the final procedure, a preliminary test was conducted on a dummy assembly using unfilled wax to validate the impregnation methodology and identify potential process challenges. An image of the magnet assembly in the impregnation vacuum chamber is shown in Figure 13a. Impregnation in vacuum eliminates air pockets and enables uniform distribution of the impregnation throughout the coil geometry, creating a rigid composite structure essential for maintaining dimensional stability during thermal cycling and electromagnetic loading. An image of the magnet assembly post-impregnation is shown in Figure13b. The extra wax at the top end of the assembly is cleaned for the final configuration.

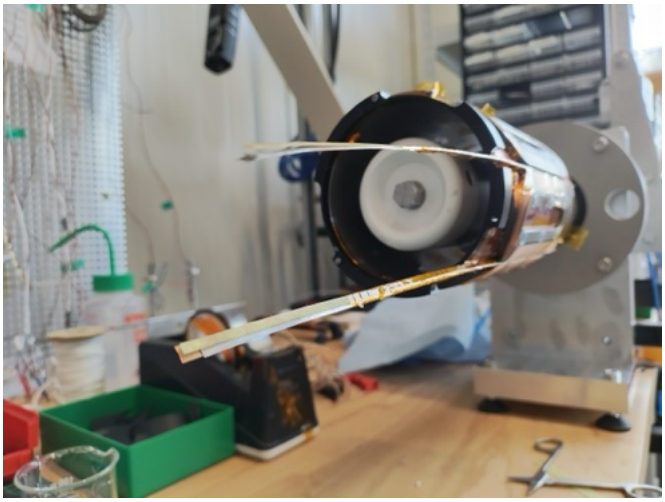

(a) Current lead assembly showing the hybrid HTS-copper conductor configuration with fiberglass mechanical reinforcement.

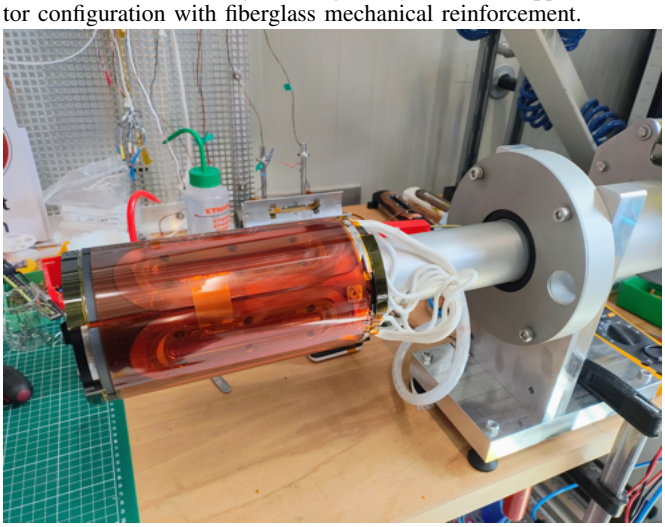

(b) Magnet assembly prepared for shell insertion showing a polyimide sheet for electrical isolation and instrumentation cables.

Fig. 12: Current lead assembly and magnet assembly preparation showing the hybrid HTS-copper conductor configuration and assembly prepared for shell insertion with protective polyimide covering for electrical isolation.

V. Test Results

This chapter presents the experimental characterization of the HTS4 cos-theta demonstrator magnet, *Ozzy*. The testing program encompasses electrical performance evaluation at nominal operating conditions, and across 30-70 K temperature range.

A. Instrumentation and Test Setup

The magnet was mounted within a vacuum cryostat with comprehensive instrumentation feed-throughs and appropriate thermal management, shown in Figure 14. The measurement setup included voltage tap monitoring across individual coils and inter-coil splice joints, current monitoring via a DC current transducer on the cables between the power supply and the cryostat, and magnetic field measurements using Hall

(a) Vacuum impregnation setup showing the magnet assembly positioned within the vacuum chamber.

(b) Completed vacuum impregnation showing the assembly fully infiltrated with alumina-filled wax.

Fig. 13: Vacuum impregnation process of the magnet assembly with alumina-filled wax to provide mechanical rigidity and thermal stability.

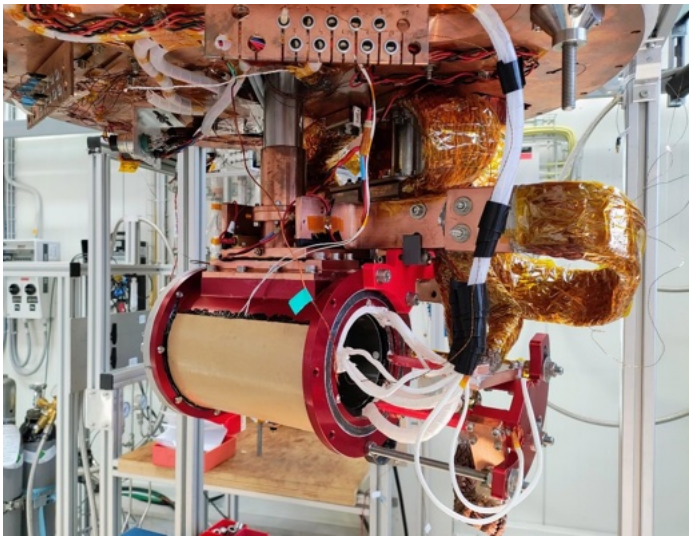

Fig. 14: Experimental setup showing the HTS4 cos-theta demonstrator magnet mounted within the cryostat.

sensors positioned within the magnet bore. A schematic of the instrumentation comprising the voltage pickups on the coils within the magnet itself is shown in Figure 15, with Hall sensor array positioning shown in Figure 16. The coil hangs directly under the second stage of a Sumitomo RDK415D GM cryocooler. The first stage of this cooler is connected to the thermal radiation shield (not shown). A second cryocooler, a 500B single-stage cools the metal current leads that transfer the current between room temperature and $\sim$50 K. 2 kA class HTS leads transfer the current between this stage and the RDK415D second stage.

The test methodology follows a three-phase characterization approach:

- **Phase 1**: Minimal characterization at 15 K to verify superconducting state
- **Phase 2**: Full characterization at 40 K nominal operating conditions
- **Phase 3**: Temperature sweep performance mapping (30-70 K)

The following sections present results from Phase 2 (40 K nominal operation) and Phase 3 (temperature sweep).

B. Electrical Performance at 40 K

The electrical characterization at 40 K represents the nominal operating condition for the HTS4 demonstrator magnet. Testing was conducted through systematic current ramping to 370 A, exceeding the design specification of 365 A, with comprehensive monitoring of voltage development across individual coils. Figure 17a shows the complete test sequence including ramp-up, plateau hold, and discharge phases. During the ramping phase, all coils exhibit inductive voltage development proportional to dI/dt, with Coil 4 consistently showing higher voltage levels. The plateau phase demonstrates stable superconducting operation with near-zero resistive voltages for five coils, while Coil 4 maintains a measurable resistive voltage component. Figure 17b presents the voltage-current relationship during ramp-up, showing linear inductive behavior for five coils and non-linear resistive contribution in Coil 4 above approximately 270 A.

Inductance analysis during the ramp-up phase at 1.0 A/s yielded coil inductance contribution of 1.25 ± 0.07 mH per coil, resulting in a total magnet inductance of 7.5 mH. Splice resistance characterization was performed using linear fits to voltage-current data over the 30-70% current range, revealing inner splice resistances of 150 ± 40 nΩ and outer splice resistances of 230 ± 70 nΩ, with an overall average splice resistance of 180 ± 60 nΩ.

At the 370 A plateau, five coils demonstrated superconducting operation with plateau voltages of 0.07 ± 0.03 mV, corresponding to coil power dissipation of 25.2 ± 12.0 mW. The total coil power dissipation was 286.2 mW, while the net magnet power (excluding current leads) measured 507 mW. Hall sensor measurements confirmed proper sextupole field generation with alternating polarity patterns and consistent transfer functions of 2.49 ± 0.04 mT/A across all sensors.

Individual coil monitoring confirmed the expected performance degradation in Coil 4 due to known tool damage sustained during the manufacturing process. This damage, documented in Figure 18, was identified prior to assembly and had already manifested as under-performance during the preliminary liquid nitrogen tests. As evident in Figure 17a, Coil 4 exhibits consistently higher voltage levels compared to the other five coils throughout the current ramping sequence. At the 370 A plateau, Coil 4 shows higher voltage levels indicating localized resistance, while the remaining coils maintain near-zero plateau voltages characteristic of superconducting operation.

Voltage-based discharge analysis yielded electromagnetic decay times of 722 ± 284 ms, exceeding the 100 ms design specification by a factor of seven (Figure 19a). These extended time constants indicate lower effective resistance than originally anticipated. The findings have significant implications for magnet protection strategies and operational cycling protocols.

Hall sensor measurements within the magnet bore revealed substantially longer magnetic field decay times of 1.5 ± 0.3 s (Figure 19b). This extended decay behavior likely reflects eddy current effects in metallic components of the magnet assembly, e.g. in the aluminum shell, which exhibit longer time constants than the primary superconducting circuit.

C. Critical Current Performance

The critical current performance of the magnet is thus limited by that of the damaged coil 4. The temperature-dependent critical current characterization was performed across the operating range from 30 K to 70 K, with results shown in Figure 20a. The experimental data demonstrates a close agreement with simulated predictions from the expected temperature dependence of the critical current of the HTS tape. The magnet achieved maximum currents of 480 A at 30 K, decreasing systematically to approximately 100 A at 70 K. The magnet was also powered up to 470 A at 20 K during the final test described later. Throughout all temperature-dependent characterization, no quench events occurred during controlled

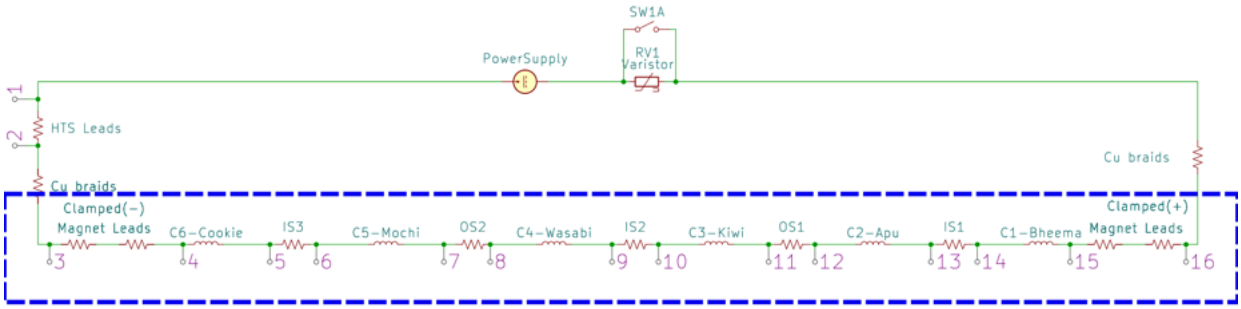

Fig. 15: Instrumentation schematic showing voltage measurement tap locations along the circuit within the cryostat, including connections for individual coils (C1-C6), inner splices (IS1-IS3), outer splices (OS1-OS2), and HTS leads configuration. The dashed-box represents the magnet.

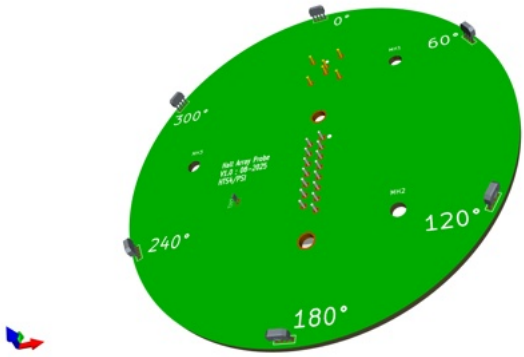

Fig. 16: Hall sensor assembly PCB showing the arrangement of magnetic field sensors positioned within the magnet bore for first-order field characterization during testing operations.

current ramping, indicating robust thermal and electromagnetic stability.

The characterization of the splice resistances across the temperature range is shown in Figure 20b. The outer splice 1 exhibited highest resistance values, ranging from 210 nΩ at 30 K to 630 nΩ at 70 K, while inner splices demonstrated lower and more stable resistance values of 120-400 nΩ across the same temperature range. Inner Splice 2 showed minimal temperature dependence, maintaining approximately 120-200 nΩ throughout the operating range. All splice resistances remained within operational limits and demonstrated consistent performance across thermal cycling, validating the splice joint design and fabrication methodology.

The final test had the goal to characterize the quench behavior of the magnet at 20 K. However, during the test, the (+) magnet current lead was compromised due to resistive heating, resulting in an open circuit condition. Post-failure examination revealed no visible macroscopic damage to the lead assembly, suggesting that the failure occurred at the electrical contact between the tapes used to construct the lead. To assess the internal state of the superconducting assembly following the test campaign, the magnet was cross-sectioned for optical examination of the coil structure, partial insulation integrity, and impregnation quality. This ongoing destructive analysis will provide critical data on the robustness of the PVB partial insulation system and wax impregnation methodology under operational thermal and electromagnetic cycling conditions.

VI. Conclusions

The cosine-theta sextupole demonstrator marks a credible way towards REBCO-based short straight sections for FCC-ee. The automated winding, relatively simple mandrel and efficient use of conductor make it a good candidate for large-scale industrial production.

The novel insulation method, in which coils are wound from coated tape and fused into monolithic blocks after winding with a short heat treatment, allows both for a well-controlled turn-to-turn resistance, as well as for easy handling of the coils during installation.

The demonstrator magnet performed according to inherent HTS tape performance limits over a temperature range of 30 K to 77 K , indicating that the cosine-theta geometry is gentle enough on the conductor. Key achievements include generating the target sextupole field of 49.8 mT at 365 A, implementation controlled turn-to-turn resistance at room temperature of $2087 \pm 74\ \mu\Omega \cdot \mathrm{cm}^2$ for passive protection, and demonstrating reproducible manufacturing with six coils.

The demonstrator did not address topics such as field quality and winding of long-length of coils. These will be tackled by the next magnet prototype - a nested cosine-theta type - to be developed by the project.

References

[1] A Abada, M Abbrescia, S S AbdusSalam, I Abdyukhanov, and Abelleira Fernandez. FCC-ee: The Lepton Collider. *The European Physical Journal Special Topics*, 228(2):261–623, 2019. ISSN 1951-6401. doi: 10.1140/epjst/e2019-900045-4. URL https://doi.org/10.1140/epjst/e2019-900045-4.

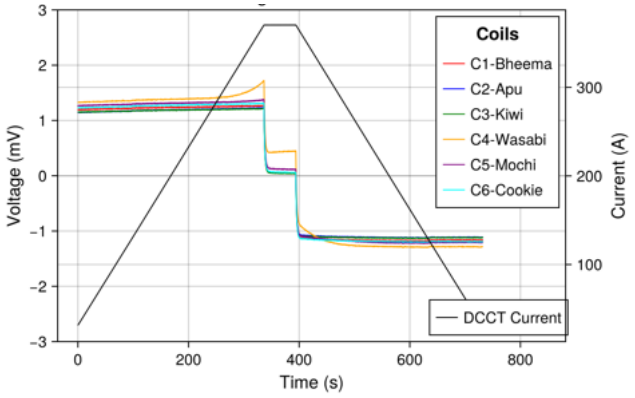

(a) Complete test sequence with current profile during ramp-up (0-300 s), plateau hold at 370 A (300-400 s), and discharge (400-800 s) phases.

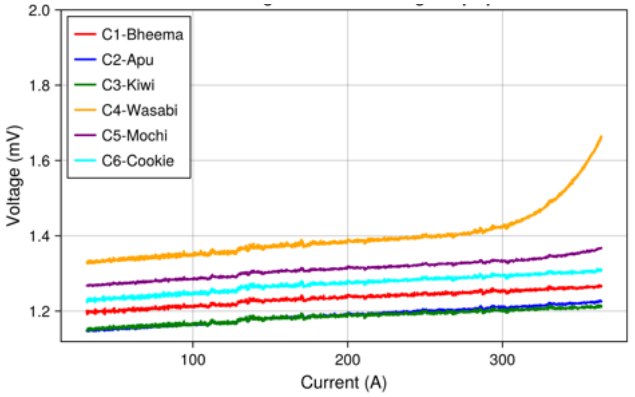

(b) Voltage-current relationship during ramp-up phase showing linear inductive response for five coils and non-linear behavior in Coil 4 above 270 A.

Fig. 17: Electrical characterization at 40 K showing coil voltage development and current ramping behavior. Coil 4 exhibits consistently higher voltage levels and non-linear resistive contribution above 270 A, indicating onset of current sharing due to manufacturing damage, while the remaining five coils maintain superconducting operation with near-zero plateau voltages.

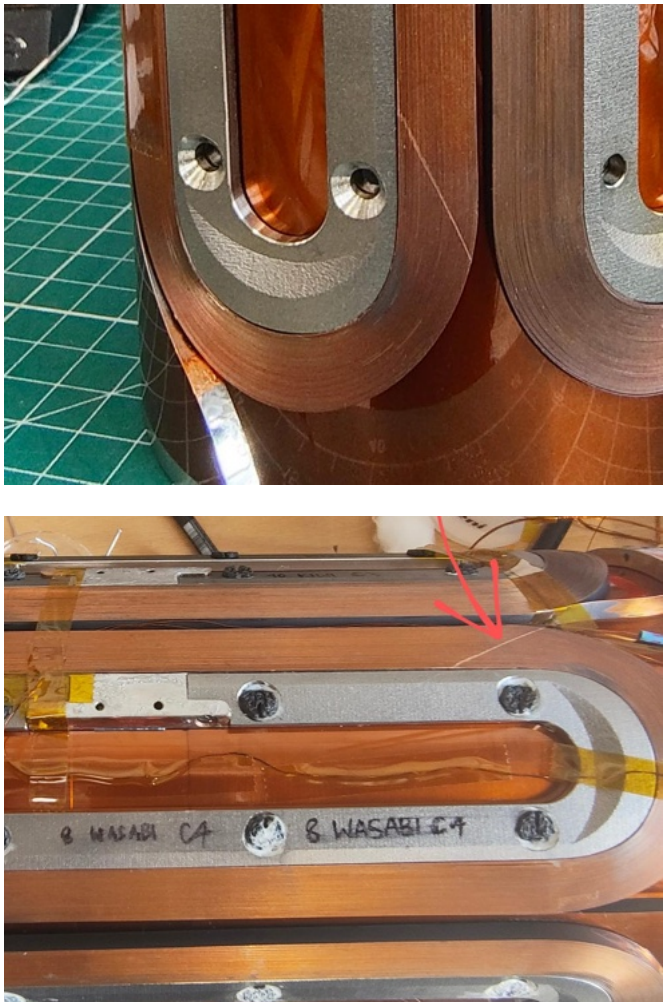

Fig. 18: Physical damage observed in Coil 4 HTS tape attributed to tool contact during manufacturing, correlating with the electrical performance degradation observed during testing.

[2] Jean Paul Burnet. UPDATE OF THE POWER DEMAND ENERGY CONSUMPTION, GRID CONNECTION FOR FCC ee. In *FCC Week 2023*, 2023.

[3] Cristobal Garcia. HTS FCC-ee energy efficient beam optics, 2023.

[4] J. Kosse, M. Koratzinos, and B. Auchmann. Reliability Engineering of Cryocooler-Based HTS Magnets for FCC-Ee. *IEEE Transactions on Applied Superconductivity*, pages 1–5, 2023. ISSN 1051-8223. doi: 10.1109/tasc.2023.3346847. URL https://ieeexplore.ieee.org/document/10373927/.

[5] Mücahid Akbas, Johann W. Kolar, and Jonas Huber. New cryogenic t-type three-switch low-voltage high-current 4q power supply for hts magnets. In *2024 IEEE Energy Conversion Congress and Exposition (ECCE)*, pages 7370–7372, 2024. doi: 10.1109/ECCE55643.2024.10861640.

[6] Cristobal Miguel Garcia Jaimes, Adrien Thabuis, Bernhard Auchmann, Jaap Kosse, Léon van Riesen-Haupt, Michael Koratzinos, Mike Seidel, Rogelio Tomas, and Tatiana Pieloni. Parameter space for the magnetic design of Nested Magnets in the FCC-ee arc cell. *JACoW IPAC*, 2024:WEPR11, 2024. doi: 10.18429/JACoW-IPAC2024-WEPR11. URL http://cds.cern.ch/record/2913742.

[7] Stephan Russenschuck. *Field Computation for Accelerator Magnets*. Wiley-VCH Verlag GmbH, 2010. ISBN 0854046356. doi: 10.1002/9783527635467.

[8] Jeroen Van Nugteren and M Danial. Parameterization of the critical surface of REBCO conductors from Bruker, 2017. URL http://cds.cern.ch/record/2277484.

[9] Stuart Wimbush. SuperOx YBCO 2G HTS, 2021.

[10] A. Molodyk, S. Samoilenkov, A. Markelov, P. Degtyarenko, S. Lee, V. Petrykin, M. Gaifullin, A. Mankevich, A. Vavilov, B. Sorbom, J. Cheng, S. Garberg, L. Kesler, Z. Hartwig, S. Gavrilkin, A. Tsvetkov, T. Okada,

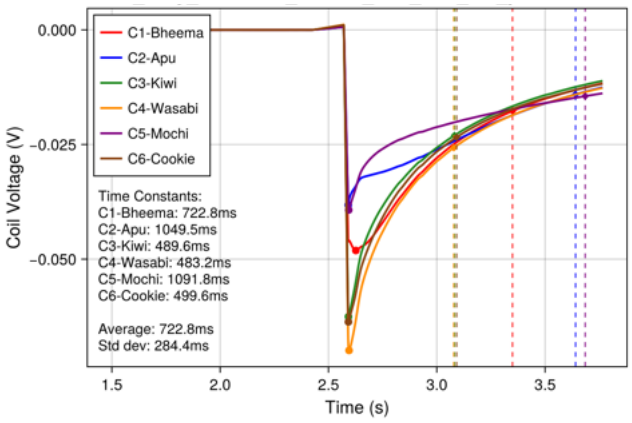

(a) High-resolution voltage-based decay analysis showing time constants of 722 ± 284 ms.

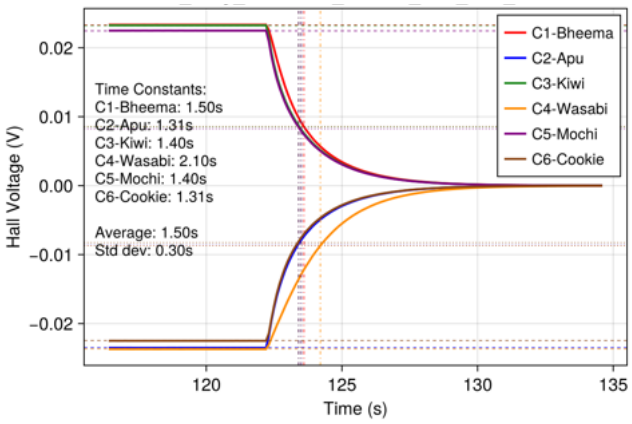

(b) Hall sensor magnetic field decay analysis showing time constants of 1.5 ± 0.3 s.

Fig. 19: Discharge time constant measurements at 40 K using high-resolution voltage measurements across individual coils and Hall sensor magnetic field decay. Results show electromagnetic decay times of 722 ± 284 ms (voltage-based), approximately 7× longer than the initial design specification of 100 ms, and 1.5 ± 0.3 s (magnetic field-based).

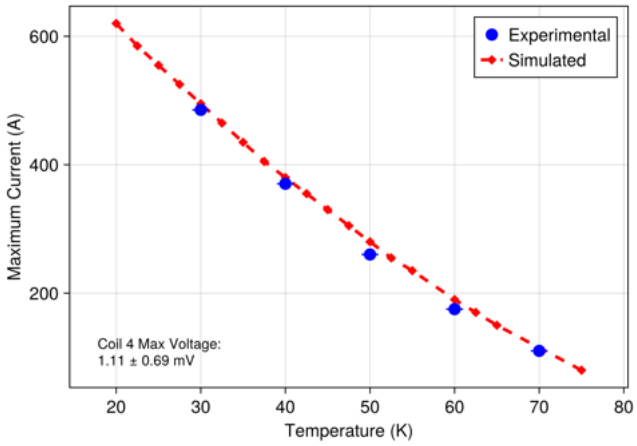

(a) Maximum current vs temperature showing experimental data compared to simulated predictions.

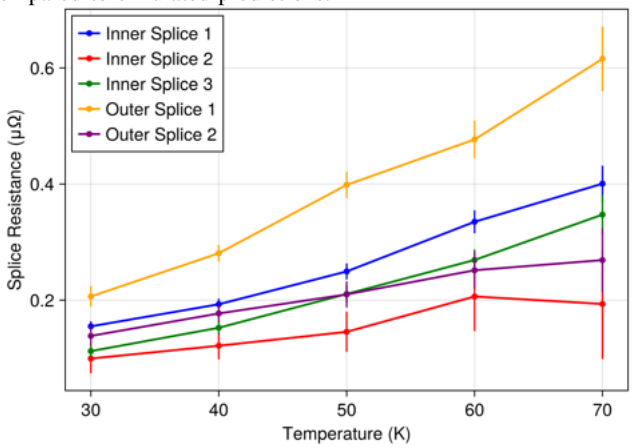

(b) Splice resistance vs temperature for inner splices and outer splices.

Fig. 20: Temperature-dependent performance characteristics showing critical current decreasing from 480 A at 30 K to approximately 100 A at 70 K with excellent agreement to simulated predictions, and splice joint resistance measurements demonstrating stable inter-coil connections with distinct temperature coefficients across the operating temperature range.

S. Awaji, D. Abraimov, A. Francis, G. Bradford, D. Larbalestier, C. Senatore, M. Bonura, A. E. Pantoja, S. C. Wimbush, N. M. Strickland, and A. Vasiliev. Development and large volume production of extremely high current density YBa2Cu3O7 superconducting wires for fusion. *Scientific Reports*, 11(1):2084, 2021. ISSN 20452322. doi: 10.1038/s41598-021-81559-z. URL https://www.ncbi.nlm.nih.gov/pubmed/33483553.

[11] Thibault Lécrevisse, Xavier Chaud, Philippe Fazilleau, Clément Genot, and Jung-Bin Song. Metal-as-insulation hts coils. *Superconductor Science and Technology*, 35 (7):074004, may 2022. doi: 10.1088/1361-6668/ac49a5. URL https://doi.org/10.1088/1361-6668/ac49a5.

[12] Elektrisola. Selfbonding wire types | ELEKTRISOLA. URL https://www.elektrisola.com/en/Products/Selfbonding-Wire/Types#europe.

[13] Matteo Crescenti, Bernhard Auchmann, André Brem, Michał Duda, Jaap Kosse, Colin Müller, Kirtana Puthran, Henrique Rodrigues, Jürgen Schmidt, and Carmine Senatore. Filled thermoplastic based coating for tailored contact resistance in HTS coils. *IEEE Transactions on Applied Superconductivity*, 2025. Under review, EUCAS 2025 Special Issue.